Modeling of plasticity-induced martensitic transformation to achieve hierarchical, heterogeneous, and tailored microstructures in stainless steels

Zhangxi Feng, Elizabeth M. Mamros, Jinjin Ha, Brad L. Kinsey*, and Marko Knezevic

Department of Mechanical Engineering, University of New Hampshire, USA

ABSTRACT

While stainless steels (SS) have excellent corrosion resistance for use in industries such as chemical and food processing, medical implants made of such steels require more stringent specifications, e.g., high strength while maintaining a low weight. A way to design and manufacture such behavior of SS is through the intentional deformation induced manipulation of constituent phases to achieve heterogeneous and hierarchical microstructures. In this paper, an elasto-plastic self-consistent modeling framework incorporating a strain-induced austenite-to-martensite transformation kinetic sub-model is calibrated using a set of SS304L data from the literature to capture stress-strain response and volume fraction of phases. The model is then validated by predicting the mechanical responses of SS316L using a new data set recorded as a function of strain-rate and temperature. By accurately predicting the material behavior, the modeling results can guide the manufacturing process to achieve the desired final part properties.

Keywords: Microstructures; Phase transformation; Formability; Crystal plasticity; Stainless steel

1. INTRODUCTION

Materials have hierarchical relationships (composition, structure, properties, and function) that vary across size scales. For example, materials often exhibit spatially differential and heterogeneous compositions, strength, wear-resistance, and porosity. Biomaterials, such as stainless steel, titanium, plastics, or composites, have applications with stringent and at times conflicting specifications such as biocompatibility, weight, chemical resistance, electrical conductivity requirements, and complex geometries. Additionally, grain size and constituents in a polycrystalline metal at the microscale hierarchically propagate the properties from the microscale to the product level. The design of these advanced materials must consider the composition at the atomic or molecular level that requires a sufficiently robust model which challenges the development of more advanced biomaterials.

Addressing major scientific challenges associated with these dual requirements for heterogeneous and hierarchical materials represents a research priority in design and manufacturing as noted by the Materials Genome Initiative [1]. Critical for these initiatives is Integrated Computational Materials Engineering (ICME) [2–5], which is used to numerically design materials, the manufacturing processes that create them, and even the final product achieved. While ICME principles have been applied to, e.g., biomaterials [6–9], typically fabricated man-made materials are homogeneous in nature. Thus, further

* Corresponding author: *E-mail address*: brad.kinsey@unh.edu (B. Kinsey).

ICME focused research to specifically address a given application, e.g., biomedical implants for trauma fixation, is required. As an example of trauma fixation hardware, see **Fig. 1**.

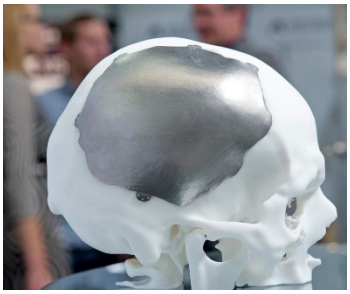

Fig. 1. Example of cranial trauma fixation hardware [10].

Certain austenitic stainless steels, e.g., SS304L and SS316L, exhibit transformation-induced-plasticity (TRIP) behaviors and are classified as biomaterials suitable for the aforementioned applications. Phase transformation is a highly localized mechanism, which creates the hierarchical, heterogeneous structures needed to satisfy the complex requirements for biomaterial applications. The deformation-induced phase transformation, from austenite to martensite, allows for increased uniform elongation, hardening, and excellent formability. Slip bands [11], stacking faults, mechanical twins, and ε-martensite [12] have the ability to form shear band intersections [12–15], which serve as the nucleation sites for strain-induced martensitic transformation [12,16–18]. The strain-induced transformation can facilitate the design of phase fractions and distributions in stainless steels by adjusting plastic deformation processes, e.g., through incremental forming or stress superposition [19,20]. In contrast, stress-assisted transformation results from existing nucleation sites introduced during the thermomechanical processing and occurs at temperatures below the martensitic transformation temperature or during elastic deformation [11,21].

Several experimental and modeling studies were conducted concerning the effects of specific parameters on the rate of strain-induced transformation in TRIP steels. Two studies focused on strain state and strain-rate effects in SS304 [22,23] with a third also including temperature effects [24]. Another study determined the deformation mode dependence of strain-induced martensitic transformation under differing temperature conditions also for SS304 [25]. Temperature and stress state were investigated for SS18-10 [26] and for TRIP780 [27]. A microstructure-based model was created focusing on the interaction energy between applied stress state and lattice deformation [28].

Stacking fault energy (SFE) is a critical intrinsic material property dependent on composition and temperature governing the kinetics of strain-induced martensitic transformation. In particular, the SFE dictates the stacking fault width (SFW) [12,29] which can generate shear bands upon being subjected to external stresses. These changes in microstructure, i.e., the formation of α'-martensite upon shear bands, alter the mechanical behavior of the steel during and upon plastic deformation [23]. Specifically, the presence of α'-martensite increases work hardening of the material whether locally or overall.

The first strain-induced martensitic transformation kinetic model was published by Olson and Cohen in 1975 [14] and describes the amount of transformation as a sigmoidal function of macroscopic strain.

Several additional kinetic models have been proposed since then that are based on this foundational work and incorporate additional parameters, such as stress triaxiality [17,30,31] or both stress triaxiality and the Lode angle parameter [26,27,32,33]. However, these models neglect to account for microstructural effects, including texture evolution and anisotropy, which are known to contribute to the martensitic transformation. Additionally, the loading path in these models is integrated through stress state parameters only, failing to capture the effect of deformation direction on the SFW [34] and the formation of shear bands [13,35–38].

In 2016, a crystal plasticity model [38], in conjunction with the Olson and Cohen kinetic model, was developed to predict the micromechanical response of polycrystalline steel. Unlike the previously mentioned models, this more complex model captures the effects of texture and anisotropy. The major limitation is that the volume fraction of martensite is a function of plastic strain only, disregarding stress state and crystal orientation. Experimental results [15] show that multiple grains can have comparable strain histories but experience different martensite transformations which contradicts the implications of this model.

Therefore, a new physics-based kinetic model was developed to predict the strain path dependence of martensitic transformation [39]. This model is also based on Olson and Cohen's previous work and was implemented into the elasto-plastic self-consistent (EPSC) crystal plasticity framework proposed and discussed in [40–49]. Predictions for martensite formation under different stress states and strain paths are achievable, and experimental results from neutron diffraction analysis of SS304L as well as additional data from the literature were used to validate this model.

Another notable dislocation-based crystal plasticity model is the open-source code DAMASK [50] that considers the kinetics of twinning and martensitic transformation of epsilon martensite, while our EPSC model considers the transformation of alpha martensite. DAMASK model considers the contribution of the ε-martensite volume fractions to dislocation density evolution through the mean-free-path estimation. This is not incorporated in our current EPSC model. Nevertheless, as new grains of α'-martensite are created, these involve the dislocation density evolution based on the set of hardening parameters for martensite. As a result, creation of the martensite grains influences the overall strain-hardening of the metal.

In this paper, the EPSC model incorporating the strain-induced austenite-to-martensite transformation kinetic sub-model is extended to model the strain-rate and temperature dependence of martensitic transformation in SS304L and SS316L. The dependence is embedded in the initial slip resistance and its evolution with the hardening law, which in combination with crystallographic orientation determines stress in the crystal [48]. The effects on the kinetics are accounted through the stress state dependence of the extended Olson-Cohen model. The temperature change arising from the plastic work during deformation is also accounted for using the method presented in [39]. The model is first calibrated using stress-strain and volume fraction data found in the literature for SS304L [47]. The framework was then validated using a new dataset of experimental stress-strain results for SS316L, accounting for temperature and strain-rate effects. Good agreement with respect to both datasets demonstrates the ability and robustness of the EPSC model to capture the mechanical response and phase fractions during deformation. Controlling the material down to the microscale through manipulation of phase transformations, and thus material constituents and properties, is an example of ICME in manufacturing. [44]

2. SUMMARY OF MODELING FRAMEWORK

A martensitic transformation model implemented in an EPSC crystal plasticity framework is used in this current work. The EPSC model was originally developed by [40] and later advanced in a number of studies [45,51]. To incorporate the phase transformation kinetics, the single crystal constitutive relation is [39]:

$$\hat{\boldsymbol{\sigma}}^c = \mathbf{C}^c\left(\dot{\boldsymbol{\varepsilon}}^c - \dot{\boldsymbol{\varepsilon}}^{pl,c} - \dot{\boldsymbol{\varepsilon}}^{pt,c}\right) - \boldsymbol{\sigma}^c tr(\dot{\boldsymbol{\varepsilon}}^c) \tag{1}$$

where $\hat{\boldsymbol{\sigma}}^c$ is the Jaumann rate of stress per crystal, $\mathbf{C}^c$ is the elastic stiffness tensor, $\dot{\boldsymbol{\varepsilon}}^{pt,c}$ is the phase transformation strain-rate, $\dot{\boldsymbol{\varepsilon}}^{pl,c}$ is the plastic strain-rate, $\dot{\boldsymbol{\varepsilon}}^c$ is the total strain-rate, and *c* enumerates each single crystal in the sample. The same constitutive equation can also be written as:

$$\hat{\boldsymbol{\sigma}}^c = \mathbf{L}^c(\dot{\boldsymbol{\varepsilon}}^c - \dot{\boldsymbol{\varepsilon}}^{pt,c}) \tag{2}$$

where $\mathbf{L}^c$ is the elasto-plastic stiffness, which is derived from the hardening law for the evolution of slip resistance, τ_c^s. The hardening law will be summarized shortly. A slip system, *s*, activates when the resolved shear stress, $\boldsymbol{\sigma}^c \cdot \mathbf{m}^s$, reaches the slip resistance, i.e., $\boldsymbol{\sigma}^c \cdot \mathbf{m}^s = \tau_c^s$ and $\hat{\boldsymbol{\sigma}}^c \cdot \mathbf{m}^s = \dot{\tau}_c^s$, where $\mathbf{m}^s$ is the Schmid tensor. An equivalent equation pertaining to the overall response of a polycrystalline aggregate is:

$$\hat{\boldsymbol{\sigma}} = \mathbf{L}(\dot{\boldsymbol{\varepsilon}} - \dot{\boldsymbol{\varepsilon}}^{pt}) \tag{3}$$

where $\hat{\boldsymbol{\sigma}}$, $\dot{\boldsymbol{\varepsilon}}$ and $\dot{\boldsymbol{\varepsilon}}^{pt}$ are the homogenized quantities for the polycrystalline aggregate, while $\mathbf{L}$ is the homogenized elasto-plastic stiffness, which is an unknown evaluated using the standard self-consistent homogenization scheme [42,52].

Mechanisms of strain-induced martensitic transformation are followed to implement phase transformation strain and crystal re-orientation [13,39,53,54]. As the volume increases by 2.59% with the transformation from austenite to martensite, which is driven by the change in lattice parameters from austenite, a_γ=0.3589 nm, to martensite, $a_{\alpha'}$=0.2873 nm [38], the transformation strain is:

$$\boldsymbol{\varepsilon}^{pt,c} = \frac{\left(\mathbf{F}^{vol}\right)^T \mathbf{F}^{vol} - \mathbf{I}}{2} \tag{4}$$

where $\mathbf{F}^{vol}$ is the deformation gradient accounting for the volume change, i.e., the volumetric portion of the Bain deformation. Crystal re-orientations from austenite {111} planes and <110> directions to α'-martensite {110} planes and <111> directions are [53]:

$$\{111\}_\gamma \parallel \{110\}_{\alpha'} \tag{5}$$

$$\langle 110\rangle_\gamma \parallel \langle 111\rangle_{\alpha'} \tag{6}$$

The underlying kinetic pertaining to the phase transformation is summarized next. The model is a crystallography-based Olson-Cohen model developed for predicting strain path sensitive martensitic transformation [13,52]. In particular, the model accounts for the effect of the stress-state at the grain-level on the evolution of martensite fraction. To this end, the Olson and Cohen (1975) model is applied at the crystal level, relating the evolution of martensite volume fraction, $f^{\alpha'}$, and the strain, :

$$f^{\alpha'} = 1 - \exp\{-\beta[1 - exp(-\alpha)]^n\} \tag{7}$$

with the fitting parameters n, α, and β to experimental data is extended to incorporate the effects of stress state using:

$$\alpha = \alpha_0 + K_\alpha \, x_\alpha(\boldsymbol{\sigma}^c) \tag{8}$$

$$\beta = \beta_0 + K_\beta \, x_\beta(\boldsymbol{\sigma}^c) \tag{9}$$

As a result, the transformation kinetics are sensitive to the crystal orientation of every grain and stress-state through components of α and β scalar parameters, respectively. α_0, β_0, K_α, and K_β are calibration parameters against the experimental data. The continued extensions were motivated by the linear dependence with the triaxiality factor proposed in [32]. The expressions for x_α and x_β are [39]:

$$x_\alpha = \sum_s \frac{\left((\hat{\mathbf{b}}_l^s - \hat{\mathbf{b}}_r^s)\boldsymbol{\sigma}^c\right)\cdot\hat{\mathbf{n}}^s}{|\boldsymbol{\sigma}^c\cdot\mathbf{m}^s| \, n_{act}} \tag{10}$$

$$x_\beta = -\frac{p}{\sigma^{eq}} \tag{11}$$

The expression for x_α stems from the mechanics of shear band formation, i.e., from the process of separation between the leading and trailing partial dislocations forming the SFW [12,37]. The condition for the formation of a shear band on a slip system, s, is $2\frac{\gamma_N}{N} - b_p\left(\left(\hat{\mathbf{b}}_l^s - \hat{\mathbf{b}}_r^s\right)\boldsymbol{\sigma}^c\right)\cdot\hat{\mathbf{n}}^s = 0$. The condition for the onset of phase transformation in the given grain, *c*, depends on the fault energy normalized by the number of intrinsic stacking faults, γ_N/N, and the forces on the partial dislocations bounding the fault. $\hat{\mathbf{b}}_l$ and $\hat{\mathbf{b}}_r$ are the Burgers directions of the left and the right partial, and $\hat{\mathbf{n}}$ is the slip plane normal. The effect of stress state is accounted for using $\left(\left(\hat{\mathbf{b}}_l^s - \hat{\mathbf{b}}_r^s\right)\boldsymbol{\sigma}^c\right)\cdot\hat{\mathbf{n}}^s$. The sum in the denominator is over the active slip systems, n_{act}. The equation is appropriately normalized by the resolved shear stress, $|\boldsymbol{\sigma}^c\cdot\mathbf{m}^s|$, to exclude the magnitude effects. The average value of the ratio $\frac{\left((\hat{\mathbf{b}}_l^s - \hat{\mathbf{b}}_r^s)\boldsymbol{\sigma}^c\right)\cdot\hat{\mathbf{n}}^s}{|\boldsymbol{\sigma}^c\cdot\mathbf{m}^s|}$ is taken over the active slip systems within a grain. For a given stress state described with the stress tensor, $\boldsymbol{\sigma}^c$, the set of active slip systems and the directions of the Burgers vectors of the partial dislocations, $\hat{\mathbf{b}}_l^s$ and $\hat{\mathbf{b}}_r^s$, and the slip plane normal, $\hat{\mathbf{n}}^s$, depend on the crystal orientation. Therefore, the x_α parameter accounts for the crystallographic effects.

The other variable, $x_\beta(\boldsymbol{\sigma})$, is defined as the ratio between the hydrostatic pressure and von Mises stress as:

$$x_\beta = -\frac{p}{\sigma^{eq}} \tag{12}$$

Once the condition for onset of transformation is fulfilled, the martensite evolution is governed by the Olson-Cohen kinetic model at the single crystal level in its incremental form. The incremental form of Eq. (7) is: $df^{\alpha'} = \left(1 - f^{\alpha'}\right)\beta n\left(f^{sb}\right)^{n-1} df^{sb}$ with $df^{sb} = \alpha\left(1 - f^{sb}\right)d\varepsilon$, where f^{sb} is the volume fraction of shear bands. The corresponding form is: $dw^{c,m} = (w_0^c - w^{c,m})\beta n\left(f^{c,sb}\right)^{n-1} df^{c,sb}$ with $df^{c,sb} = \alpha\left(1 - f^{c,sb}\right)\sum_s d\gamma^s$, where w_0^c is the initial volume fraction of the parent austenite grain, and $w^{c,m}$ is the volume fraction of the product, i.e., the martensite grain. The sum of shear strains on slip systems, $\sum_s d\gamma^s$, relates the strain to the evolving fraction of martensite in the single crystal version of the Olson-Cohen law. Therefore, the volume fraction of martensite for each austenite crystal evolves as a function of deformation mechanism, i.e., the shear strain per crystal. The volumetric part of strain is accounted for

using Eq. (4). Once the volume fraction of martensite reaches 1% of the parent austenite grain, a new grain is created and added to the polycrystalline aggregate. Numerical aspects pertaining to the implementation of the model in EPSC are discussed in [45].

The strain-rate and temperature sensitive hardening law used for the evolution of slip resistance is summarized next. The evolution of resistance to slip is defined using:

$$\dot{\tau}_c^{c,s} = \sum_{s'} h^{ss'} \dot{\gamma}^{c,s'} \tag{13}$$

where $h^{ss'}$ is the hardening matrix and $\dot{\gamma}^{c,s}$ is the shearing rate per system, *s, s'*. The hardening matrix is then:

$$h^{ss'} = \frac{\partial \tau_c^s}{\partial \gamma^{s'}} \tag{14}$$

The resistance to slip on a slip system involves several terms [55]:

$$\tau_c^s = \tau_0^\alpha + \tau_{forest}^s + \tau_{debris}^\alpha \tag{15}$$

where α enumerates a slip family and τ_0^α is an initial slip resistance defined using:

$$\tau_0^\alpha(\dot{\varepsilon}, T) = A^\alpha(1 + B^\alpha \, log(\dot{\varepsilon}))exp(-\frac{T}{C^\alpha}) \tag{16}$$

with A, B, and C as fitting constants. T is temperature in Kelvin. τ_{forest}^s is a forest term governing the contribution from the statistically stored dislocations:

$$\tau_{forest}^s = b^\alpha \chi \mu^\alpha \sqrt{\sum_{s'} L^{ss'} \rho_{tot}^{s'}} \tag{17}$$

where b^α is the Burgers vector, $\chi = 0.9$ is an interaction constant, μ^α is the shear modulus, ρ_{tot}^s is the forest dislocation density per slip system ($s \in \alpha$), and $L^{ss'}$ is a strength interaction matrix with entries set to 1 [56,57], s indicates the interaction with the system itself while s' indicates the interaction with all the other slip systems. τ_{debris}^α is a debris term governing a contribution from dislocations stored as debris terms [55]:

$$\tau_{debris}^\alpha = 0.086 \, \mu^\alpha b^\alpha \sqrt{\rho_{deb}} log\left(\frac{1}{b^\alpha \sqrt{\rho_{deb}}}\right) \tag{18}$$

where ρ_{deb} is the debris dislocation density [58].

$\rho_{tot}^{s'}$ and ρ_{deb} evolve with shearing strain on the slip systems according to the evolution laws [57–59]:

$$\frac{\partial \rho_{tot}^s}{\partial \gamma^s} = k_1^\alpha \sqrt{\sum_{s'} g^{ss'} \rho_{tot}^{s'}} - k_2^\alpha(\dot{\varepsilon}, T) \rho_{tot}^{s'} \tag{19}$$

in which k_1^α determines the rate of generation of dislocations, while k_2^α determines dynamic recovery [60]. $g^{ss'}$ is a matrix governing the slip system interactions [57,61,62]. Here the diagonal form of the $g^{ss'}$ matrix was adopted, i.e., $g^{ss} = 1$ and $g^{ss'} = 0$. The initial total dislocation density is set to $10^{11} \, m^{-2}$. While k_1^α is a fitting constant, k_2^α is defined in terms of temperature and strain-rate as [63]:

$$\frac{k_2^\alpha}{k_1^\alpha} = \frac{\chi b^\alpha}{g^\alpha}\left(1 - \frac{k_B T}{D^\alpha (b^\alpha)^3} ln\left(\frac{\dot{\varepsilon}}{\dot{\varepsilon}_0}\right)\right) \tag{20}$$

where k_B, $\dot{\varepsilon}_0 = 10^7\ s^{-1}$, g^α, and D^α are the Boltzmann constant, a reference strain-rate, an effective activation enthalpy, and a drag stress, respectively. The debris dislocation density in the grain evolves with shear strain on the slip systems as:

$$\frac{\partial \rho_{deb}}{\partial \gamma^s} = q^\alpha b^\alpha \sqrt{\rho_{deb}}\, k_2^\alpha(\dot{\varepsilon}, T)\rho_{tot}^s \tag{21}$$

where q^α is a dislocation recovery rate constant. The initial debris dislocation density is 0.1 m^{-2}.

3. RESULTS AND DISCUSSION

This section details the calibration of the EPSC model for simulating the phase transformation effects for both SS304L and SS316L materials. The experimental data for SS304L are taken from literature while the data for SS316L was measured. This section first discusses the results of calibrating the model for SS304L and then presents the experimental data and model calibrations for SS316L.

3.1. Model Calibration Using SS304L Data from Literature

The strain-rate and temperature sensitive initial slip resistance law, Eq. (16), was added to the EPSC framework with the extended Olson-Cohen model. The updated model was first calibrated with literature data on SS304L showing strain-rate effects on stress-strain response and transformation behavior [47]. As both materials, SS304L and SS316L, were in the form of rolled sheets and are similar in microstructure, the measured texture of SS316L was used for modeling of SS304L as well. Pole figures showing the initial texture measured by neutron diffraction of the as-rolled sheet are shown in **Fig. 2**. The labelled max values indicate maximum intensity per pole figure. Note that the pole figure are labeled as {200}, {220} and {222} as these give rise to the diffraction, while Eqs. (5) and (6) used the equivalent reduced notation of the indices.

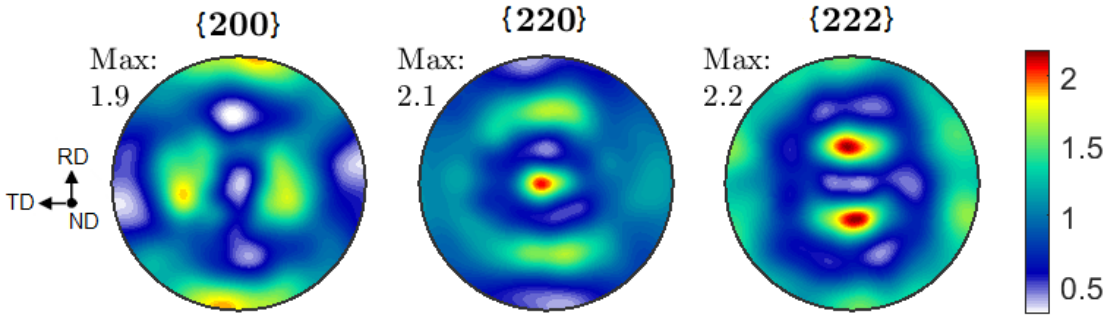

Fig. 2. Pole figures showing the initial texture of SS316L sheet measured by neutron diffraction and used for simulations of both SS304L and SS316L.

In [47], SS304L sheets were commercially produced, annealed, and temper rolled after the final heat treatment to a nominal thickness of 1.5 mm. The volume fraction data was measured using X-ray diffraction. The tensile sheets were strained to fracture in the rolling direction (RD) at room temperature of 24 °C ± 1 °C. The martensite volume fraction during the deformation process at strain rates of 1.25 e-4 s^{-1}, 0.125 s^{-1}, and 100 s^{-1} were obtained through interrupted tensile tests.

In EPSC, a material loaded with a tensile force in the rolling direction was simulated by imposing normal strain increments in the tensile direction while enforcing the normal stresses in the lateral directions. All the shear strains were set to be zero. **Figure 3** shows the comparisons between the simulated and measured stress-strain responses and volume fraction evolutions of α'-martensite in SS304L. The experimental values were measured using x-ray diffraction [47].

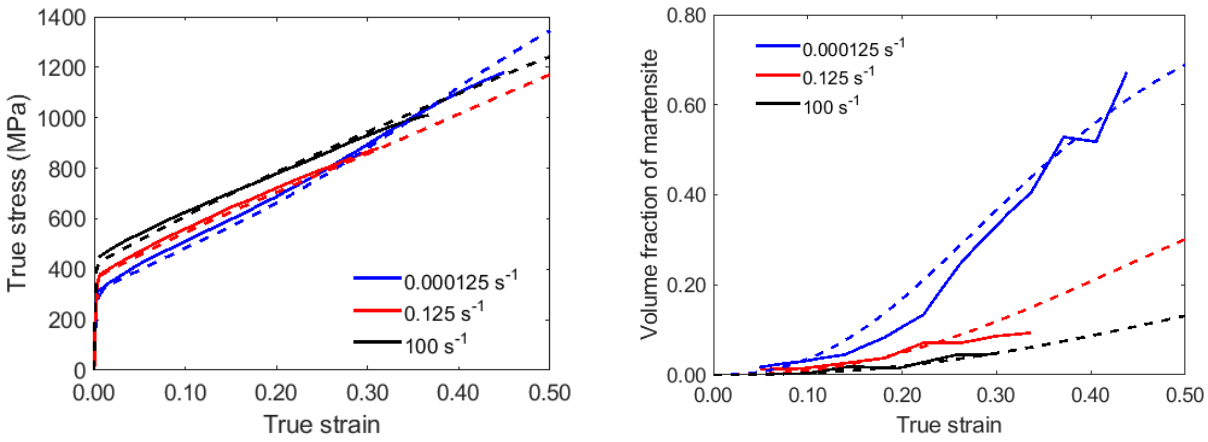

Fig. 3. Comparison of the simulated (dash lines) and measured (solid lines) mechanical responses (left) and evolution of α'-martensite volume fractions (right) for three strain-rates as specified in the legends for SS304L.

The calibration of hardening parameters and the kinetic model of each austenite and martensite phase was completed in three steps. First, the initial slip resistance constants for austenite were determined. The fitting constants B and C from Eq. (16) were set to 0 and 1e6, respectively, to remove the temperature and strain-rate effects. The value 1e6 is an arbitrarily large number to set the exponential term to approximately 1. Then, the initial slip resistances were obtained by fitting the initial plastic slope of the stress-strain curves. This produced the initial slip resistances for austenite, τ_0^γ, at each strain-rate since contribution from martensite is negligible at the onset of yielding. Then, taking the ratio of Eq. (16) using two strain-rates, constant B was calibrated:

$$\tau^{\gamma}_{0\_\dot{\varepsilon}_1}(\dot{\varepsilon}_1, T = 298\ K) = A^{\gamma}(1 + B^{\gamma}\log(\dot{\varepsilon}_1))\exp\left(-\frac{T}{C^{\gamma}}\right) \tag{22}$$

$$\tau^{\gamma}_{0\_\dot{\varepsilon}_2}(\dot{\varepsilon}_2, T = 298\ K) = A^{\gamma}(1 + B^{\gamma}\log(\dot{\varepsilon}_2))\exp(-\frac{T}{C^{\gamma}}) \tag{23}$$

$$B^{\gamma} = \frac{\left(\tau^{\gamma}_{0_{\dot{\varepsilon}_1}}/\tau^{\gamma}_{0_{\dot{\varepsilon}_2}} - 1\right)}{\log(\dot{\varepsilon}_1) - (\tau^{\gamma}_{0_{\dot{\varepsilon}_1}}/\tau^{\gamma}_{0_{\dot{\varepsilon}_2}})\log(\dot{\varepsilon}_2)} \tag{24}$$

Three values of B were calculated by comparing all strain-rates with each other and the average value was used. Since this data is at room temperature only, the SS316L data was used to calibrate constant C using Eq. (25), derived from taking the ratio of Eq. (16) using two temperatures. Then, constant A was solved as the only unknown remaining in the equation.

$$\frac{\tau^{\gamma}_{0\_T_1}}{\tau^{\gamma}_{0\_T_2}} = \frac{\exp\left(-\frac{T_1}{C^{\gamma}}\right)}{\exp(-\frac{T_2}{C^{\gamma}})} => C^{\gamma} = \frac{-T_1+T_2}{\log(\tau^{\gamma}_{0_{T_1}}/\tau^{\gamma}_{0\_T_2})} \quad (25)$$

Second, the extended Olson-Cohen model's coefficients from Eqs. (8) and (9) were adjusted to match the volume fraction evolution of the α'-martensite. The final phase transformation parameters are listed in **Table 1**. The stress state coefficient β_0 is fitted for the volume fraction data to account for the effect of the three strain-rates of the SS304L literature data shown in **Fig. 3**.

Lastly, other hardening parameters for austenite and martensite were fitted. The literature data included flow curves at strain-rates of $1.25e^{-3}$, $1.25e^{-2}$, 1.25, 10, and $400\ s^{-1}$. The austenite hardening parameters were calibrated by fitting the flow curves of strain-rates higher than $0.125\ s^{-1}$ as the flow stress contribution from martensite is negligible. Then, the martensite parameters were calibrated by fitting the flow curves at strain-rates of $1.25e^{-3}$ and $1.25e^{-4}\ s^{-1}$. The rest of the data can be regarded as predictions.

The final hardening parameters are listed in **Table 2**. As the model is elasto-plastic, the crystal elastic constants for austenite are $C_{11} = 209\ GPa$, $C_{12} = 133\ GPa$, and $C_{44} = 121\ GPa$, while those for martensite are $C_{11} = 234\ GPa$, $C_{12} = 135\ GPa$, and $C_{44} = 118\ GPa$ [38]. The $\{1\bar{1}1\}\langle 110\rangle$ and the $\{110\}\langle 1\bar{1}1\rangle$ slip systems are used for austenite and martensite, respectively. Since the literature SS304L data do not have temperature dependence, parameter C^{α} was initially set to an arbitrary large value of 1e6 to not consider the effect of temperature. After the SS316L data was modeled, parameter C^{α} for the SS316L was used for SS304L as their mechanical behaviors are very similar, and parameters A^{α} and B^{α} were adjusted accordingly. The final parameters are shown in **Table 2**.

Table 1. Phase transformation parameters of austenite and martensite phases for modeling the SS304L (literature data from [47]).

α_0	K_{α}	β_0	K_{β}	n	$\frac{\gamma_N}{N}\ [\frac{mJ}{m^{-2}}]$	$f_{cr}^{\alpha'}$
0.5	0.3	5.0 @ $\dot{\varepsilon}_1 = 0.000125\ s^{-1}$ 1.2 @ $\dot{\varepsilon}_2 = 0.125\ s^{-1}$ 0.3 @ $\dot{\varepsilon}_3 = 100\ s^{-1}$	1.0	2.5	1.0	0.00001

Table 2. Hardening law parameters of austenite and martensite phases for modeling the SS304L (literature data from [47]).

Phase	$A^{\alpha}[MPa]$	B^{α}	$C^{\alpha}[K]$	$k_1\ [m^{-1}]$	g	$D\ [MPa]$	q	b [Å]
γ	394.0	0.024	251.7	0.68×10^8	0.12	100	4	2.54
α'	800.0	0.0283	589.0	1.00×10^8	0.25	100	4	2.49

Additionally, the literature also provided data for predicting the temperature change during an adiabatic deformation with the equation [47]:

$$\Delta T = \beta \frac{\int_0^{\varepsilon_f} \sigma_{ave} d\varepsilon}{\rho C_p} \tag{26}$$

where ε_f is the final strain, σ_{ave} is the average stress in each strain increment, $\rho = 8.03\ \frac{g}{cm^3}$ is the density of SS304L, $C_p = 0.5\ \frac{J}{g°C}$ is the specific heat, and $\beta = 0.95$ is the fraction of deformational work converted to heat. These values are also inherited from the literature [47]. Adiabatic deformation is defined as a deformation process at strain-rates higher than $0.1\ s^{-1}$ to avoid excess heat transfer with the environment. With this relationship implemented in the EPSC framework, this change in temperature can be used to update the behavior of the material at every step. **Figure 4** shows the comparisons between the simulated and measured temperature change during an adiabatic process with an initial temperature of 25 °C. The temperatures were measured by welding thermocouples to the gage sections [47].

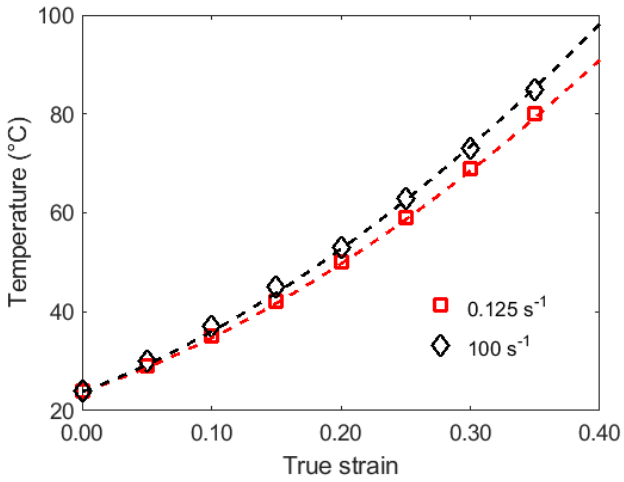

Fig. 4. Comparison of the simulated (dash lines) and measured (data points) temperature change during adiabatic deformation process along the RD for SS304L (strain-rates greater than $0.1\ s^{-1}$).

3.2. SS316L Experiments

Knowing the strain-rate and temperature dependences of a similarly SS304L from the literature, uniaxial tension experiments were conducted to determine these dependences for SS316L, which is also used in this research.

Experiments were performed to characterize the material properties from various perspectives: (1) strain-rate and (2) temperature effects on the flow stress and (3) plastic anisotropy evolution with respect to the plastic work. The former, i.e., (1) and (2), were performed only along the rolling direction (RD) with (1) at room temperature and (2) under regulated temperature conditions, i.e., “isothermal”, while the latter, i.e., (3), was conducted along RD, 45°, and transverse direction (TD) at room temperature.

To control the temperature conditions during experiments, a compressor (Thermo Fisher), pump (Thermo Fisher), and heat exchanger (AAVID) were combined to create an “isothermal” temperature regulation system utilizing a 60% ethylene glycol/40% water mixture as the circulating fluid. Note that isothermal is

used in quotations because temperature gradients were evident as the specimens approached fracture. The temperature rating for the overall system is -50°C to 200°C, but the fluid choice restricted the lowest possible temperature setting to -30°C. To verify that the specimens reached the desired steady-state temperatures prior to testing, a thermocouple was used, and adjustments were made to the system's temperature setting as necessary. Uniaxial tensile specimens were waterjet cut from 1.2 mm thick sheets of SS316L following the ASTM E8 standard, with gauge length (GL) dimensions of 82.15 mm for (1) and (3) versus 57 mm for (2), as shown in **Fig. 5**. This change in GL to the minimum stated in the standard was necessary to accommodate the heat exchanger to ensure that the entire GL remained in contact throughout the experiment. The experiments were conducted on a MTS Landmark machine with a 250 kN load cell incorporated. For strain-rate effect experiments, pulling speeds of 0.1, 0.01, 1, 0.5 and 10 mm/s were prescribed corresponding to initial strain-rates of approximately 1e-3, 1e-4, 1e-2, 5e-3, and 1e-1 s^{-1}, respectively. Based on these results, the strain-rate sensitivity coefficient, i.e., *m,* was calculated as approximately 0.032 using:

$$\frac{\Delta\sigma}{\bar{\sigma}} \cong m \ln\left(\frac{\dot{\varepsilon_2}}{\dot{\varepsilon_1}}\right) \tag{27}$$

where σ is the true stress, $\bar{\sigma}$ is the equivalent stress, and $\dot{\varepsilon_1}, \dot{\varepsilon_2}$ are different strain rates.

For temperature effect experiments in (2), a pulling speed of 0.1 mm/s was prescribed (approximately 1e-3 s^{-1}). A clamp was used to mount the specimens to the heat exchanger near the bottom, stationary MTS grip as shown in **Fig. 6**. Corkboard was placed between the heat exchanger and MTS grips to prevent direct contact. To ensure uniform contact between the specimen and heat exchanger, a <50 N out-of-plane force was applied behind the heat exchanger.

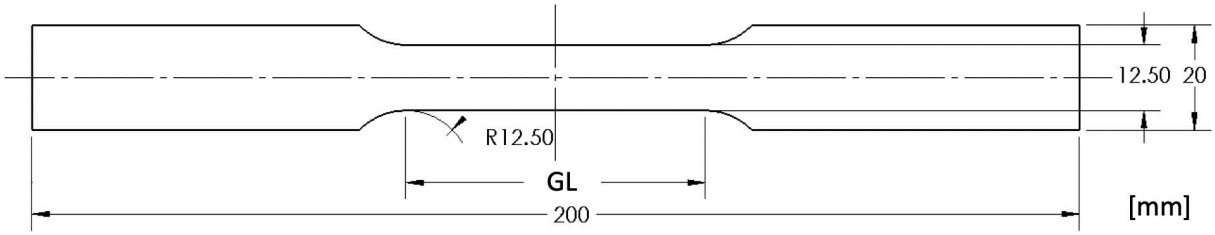

Fig. 5. Uniaxial tensile specimens obtained from 1.2 mm thick SS316L.

Stereo type digital image correlation (DIC), i.e., 3D-DIC, consisting of two FLIR 5.0 megapixel cameras with 17 mm Schneider Xenoplan compact lenses, and a FLIR SC-645 infrared (IR) camera (temperature range of -20°C to 650°C with a resolution of 0.05°C) were utilized to simultaneously measure strain and temperature, respectively, *in-situ.* All three cameras were coupled using VIC Snap (Correlated Solutions Inc.) to capture synchronously at 2 Hz. A black and white speckle pattern was spray painted on the specimen surfaces for this purpose, and a corresponding emissivity of 0.98 was used based on calibrations with a thermocouple.

The acquired images were post-processed using VIC-3D (Correlated Solutions Inc.) with subset and step sizes of 17 and 4 pixels, respectively. The area of interest included the entire gauge length with an inspect rectangle encompassing the fracture region and an inspect point at the center of the fracture to analyze strain and temperature data.

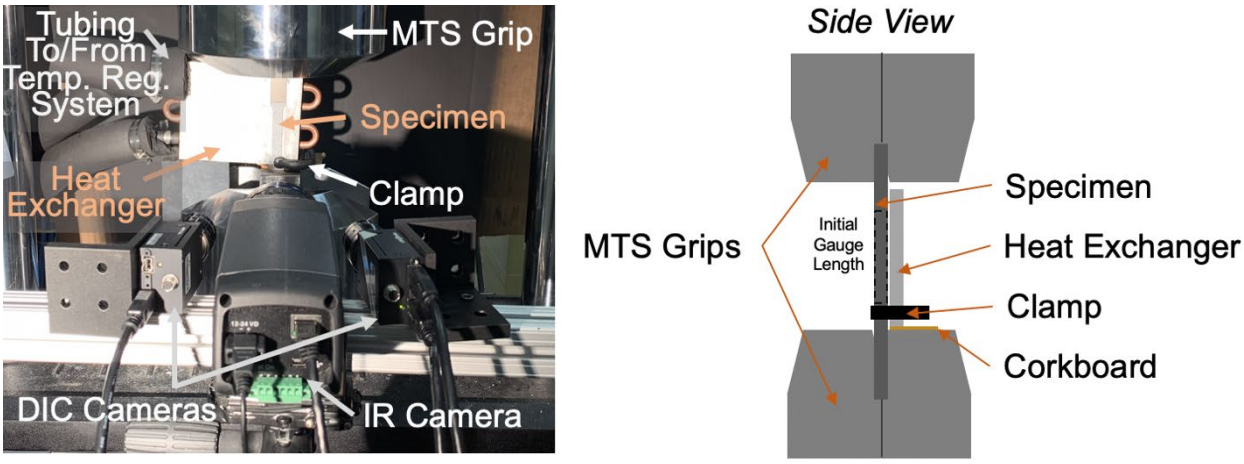

Fig. 6. Experimental setup with DIC, IR camera, "isothermal" temperature regulation system, and MTS grips (adapted from [49]).

To capture the plastic anisotropy in the flow stress of SS316L, the stress ratios were calculated using:

$$\text{stress ratio} = \frac{\sigma}{\bar{\sigma}} \tag{28}$$

where σ is the true stress and $\bar{\sigma}$ is the equivalent stress, which is assumed as the true stress from the uniaxial tension in the RD experiment, i.e., the normalized true stress. See **Fig. 7** for a plot of the corresponding stress-strain curves for each specimen orientation in addition to the simulated values. The model predicts the stress-strain responses for RD and 45° well and underpredicts TD. The measured texture has 24961 grains representing their respective orientations. The texture was systematically reduced to 500 grains to preserve the overall texture pattern using a generalized spherical harmonics algorithm [64]. The texture is reduced to allow the EPSC to complete the simulation in a reasonable amount of time as the model iterates through each grain and solves their properties such as stress and martensite volume fraction evolution. Since these results are highly dependent on the input texture data, the difference in TD can be a result of the reduction process or possible missing TD peaks during the measurement.

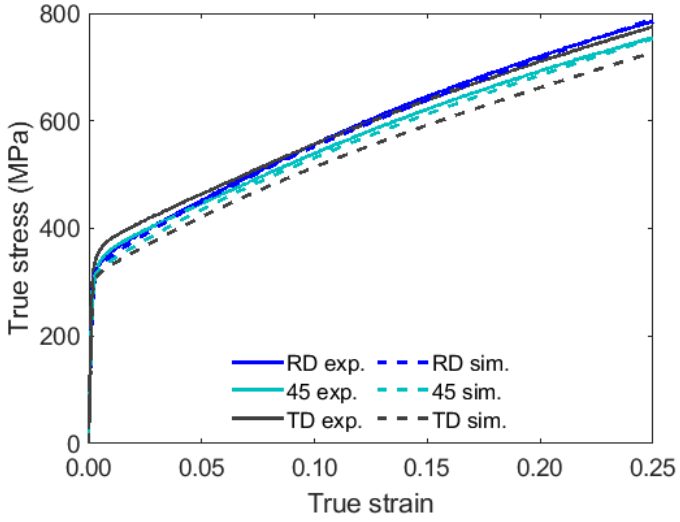

Fig. 7. Comparison of measured and simulated true stress-strain curves for uniaxial tension in RD, 45°, and TD for SS316L.

The r-values, so called Lankford coefficients, were also calculated for each specimen orientation using:

$$\text{r-value} = \frac{d\varepsilon_w^{pl}}{d\varepsilon_t^{pl}} \tag{29}$$

where ε_w^{pl} is the plastic width strain, ε_t^{pl} is the plastic thickness strain, and d represents the increment in each subsequent parameter. The r-values are used to characterize the plastic anisotropy in the uniaxial tension of sheet materials. As per Eq. (29), the r-value indicates the resistance to thinning and thus relates to the formability of the material.

In the experiments, since the incremental strains measured by DIC have unavoidable noise at the high data acquisition rate, the r-values were calculated in an averaging scheme, by computing the strain increment from every 10 data points, and then the resulting data set was smoothed in MATLAB using a locally weighted linear regression. See **Fig. 8** for a plot of the corresponding experimental and simulated r-values with error bars representing the maximum and minimum values from three experiments and confirming repeatability. Data from the plastic work range of approximately 1 to 150 MJ/m^3, corresponding to an equivalent plastic strain range of 0.004 to 0.25, are shown to eliminate any error from the elastic to plastic transition at small plastic work values and strain localization towards the end of the experiment.

The material orientation has a significant influence on the r-values while a minor effect on the stress-strain results. This can be explained by the measured texture of the material represented by the pole figures in **Fig. 2**. The directionality of the rolling process causes mechanical fibering and as a result, there is a lack of preferred crystallographic orientation in TD as visualized by a lack of peak intensities. The model predicts the r-values in the RD and 45^o in a reasonable agreement, but overpredicts the TD. While r-values are not predicted well for the TD orientation in **Fig. 8**, the stress-strain responses presented in **Fig. 7** are reasonable.

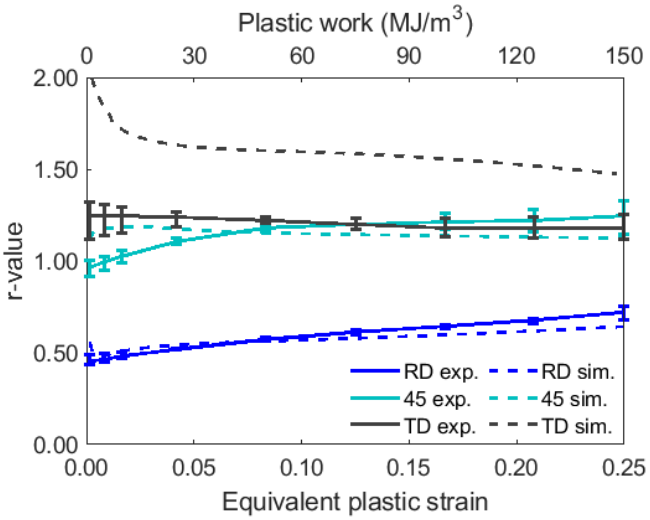

Fig. 8. Comparison of simulated and measured evolution of r-values over selected equivalent plastic strain and work ranges for RD, 45°, and TD for SS316L.

3.3. Model Verification using SS316L Measured Data

Using the temperature-dependent data for SS316L, Eq. (25) was used to calibrate constants C^a in Eq. (16). Then, the strain-rate dependent data and Eq. (24) were used to calibrate constants B^a. Finally, constants A^a were calculated as the last unknown constant. The averages of the values from each data set were taken as the final values and are listed in **Table 3**. The 0°C and 1e-3 s^{-1} stress-strain curves were used to calibrate the model by adjusting parameters from the values used for modeling the SS304L data. The other curves are predicted results using the same parameters and changing boundary conditions such as temperature and strain rate.

For the phase transformation parameters, it has been observed that the martensitic phase transformation processes in SS304L and SS316L both follow the sigmoidal shape and were modeled with the Olson-Cohen equation. Furthermore, SS316L transforms at a lower rate than SS304L under the same temperature and loading conditions [30,65]. Since phase characterization data was unavailable for SS316L, the phase transformation parameters of SS304L at $0.125\ s^{-1}$ strain-rate was used to represent a lower rate of transformation. The fitted curves and measured data are shown in **Fig. 9**. The model predicts the effect of strain rate and temperature on the mechanical responses of the materials well, demonstrating the strengthening effect of the material under higher strain rates and the softening effect of the material under higher temperatures. The SS316L material exhibits a weak strain-rate sensitivity of 0.03, and a more significant temperature dependence at higher strain levels.

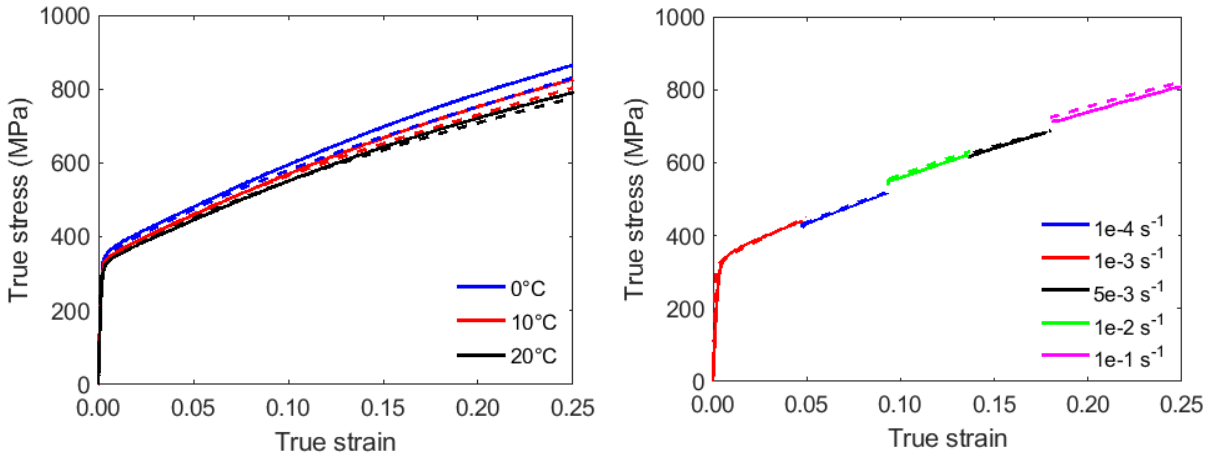

Fig. 9. Temperature (left, at 0.001 s^{-1}) and strain rate (right, at 20°C) effects on the flow stress-strain curves in uniaxial tension in RD and comparison of the simulation (dashed lines) and experiment (solid lines) for SS316L.

Table 3. Hardening law parameters for austenite and martensite of SS316L.

Phase	$A^{\alpha}[MPa]$	B^{α}	$C^{\alpha}[K]$	$k_1\ [m^{-1}]$	g	$D\ [MPa]$	q	b [Å]
γ	328.0	0.015	251.7	1.4×10^8	0.11	100	4	2.54
α'	700.0	0.0283	589.0	1.00×10^8	0.25	100	4	2.49

4. CONCLUSIONS AND FUTURE WORK

In this research, mechanical tests over a range of strain-rates and temperatures were conducted to study the mechanical response of SS316L. The experimental results were then modeled using the EPSC framework after first calibrating the model using uniaxial tension data for SS304L from [47]. The framework incorporates an extended Olson-Cohen model to predict transformation-induced plasticity effects of strain-induced martensitic phase transformation. A plastic work to temperature conversion relationship was implemented to predict the increase in temperature during plastic deformation. The strain-rate sensitive martensite evolution of SS304L was predicted. The texture of the SS316L specimen was measured and used in the simulations. The stress strain curves and r-values of uniaxial tension tests in the RD, 45°, and TD were compared with the predictions for SS316L. Good agreement between experimental and modeling datasets for SS304L and SS316L demonstrate the robustness of the developed crystal plasticity model. The evolution of martensitic phase transformation at different strain levels forms tailored microstructures to achieve hierarchical and heterogeneous material compositions in stainless steels. In future work, the EPSC model will be coupled with finite element method software packages [44] that enable simulations of more complex deformation processes, e.g., biaxial loading, incremental

forming, strain path changes, and continuous bending. These simulations will be utilized to predict phase evolutions over complex geometries to allow designs that achieve spatially differential properties.

Acknowledgments

This research was sponsored by the U.S. National Science Foundation and was accomplished under the Grant No. OIA-1757371.

REFERENCES

[1] National Science and Technology Council, 2014, *Materials Genome Initiative Strategic Plan*.

[2] Center for Hierarchical Materials Design, 2016, *Annual Report*.

[3] National Research Council, 2008, *Integrated Computational Materials Engineering: A Transformational Discipline for Improved Competitiveness and National Security*.

[4] The Minerals Metals and Materials Society, 2013, "Integrated Computational Materials Engineering (ICME): Implementing ICME in the Aerospace, Automotive, and Maritime Industries, a Study Organized by TMS."

[5] W.D. Callister Jr, D. G. R., 2012, *Fundamentals of Materials Science and Engineering: An Integrated Approach*, John Wiley & Sons.

[6] Gronau, G., Krishnaji, S. T., Kinahan, M. E., Giesa, T., Wong, J. Y., Kaplan, D. L., and Buehler, M. J., 2012, "A Review of Combined Experimental and Computational Procedures for Assessing Biopolymer Structure–Process–Property Relationships," Biomaterials, **33**(33), pp. 8240–8255.

[7] Hollister, S. J., and Lin, C. Y., 2007, "Computational Design of Tissue Engineering Scaffolds," Computer Methods in Applied Mechanics and Engineering, **196**(31), pp. 2991–2998.

[8] Lee, N., Horstemeyer, M. F., Rhee, H., Nabors, B., Liao, J., and Williams, L. N., 2014, "Hierarchical Multiscale Structure–Property Relationships of the Red-Bellied Woodpecker (Melanerpes Carolinus) Beak," Journal of The Royal Society Interface, **11**(96), p. 20140274.

[9] Meyers, M. A., and Chawla, K. K., 1984, *Mechanical Metallurgy: Principles and Applications*.

[10] Crane, J., Crestani, R., and Cotteleer, M., 2014, "3D Opportunity for End-Use Products: Additive Manufacturing Builds a Better Future," Deloitte Rev., **14**.

[11] Das, Y. B., Forsey, A. N., Simm, T. H., Perkins, K. M., Fitzpatrick, M. E., Gungor, S., and Moat, R. J., 2016, "In Situ Observation of Strain and Phase Transformation in Plastically Deformed 301 Austenitic Stainless Steel," Materials & Design, **112**, pp. 107–116.

[12] Talonen, J., and Hänninen, H., 2007, "Formation of Shear Bands and Strain-Induced Martensite during Plastic Deformation of Metastable Austenitic Stainless Steels," Acta Materialia, **55**(18), pp. 6108–6118.

[13] Olson, G. B., and Cohen, M., 1972, "A Mechanism for the Strain-Induced Nucleation of Martensitic Transformations," Journal of the Less Common Metals, **28**(1), pp. 107–118.

[14] Olson, G. B., and Cohen, M., 1975, "Kinetics of Strain-Induced Martensitic Nucleation," Metallurgical Transactions A, **6**(4), p. 791.

[15] Polatidis, E., Hsu, W.-N., Šmíd, M., Panzner, T., Chakrabarty, S., Pant, P., and Van Swygenhoven, H., 2018, "Suppressed Martensitic Transformation under Biaxial Loading in Low Stacking Fault Energy Metastable Austenitic Steels," Scripta Materialia, **147**, pp. 27–32.

[16] Olson, G. B., and Azrin, M., 1978, "Transformation Behavior of TRIP Steels," Metallurgical Transactions A, **9**(5), pp. 713–721.

[17] Haidemenopoulos, G. N., Aravas, N., and Bellas, I., 2014, "Kinetics of Strain-Induced Transformation of Dispersed Austenite in Low-Alloy TRIP Steels," Materials Science and Engineering: A, **615**, pp. 416–423.

[18] Kuroda, Y., 1987, "Kinetics of Deformation-Induced Transformation of Dispersed Austenite in Two Alloy Systems."

[19] Meya, R., Löbbe, C., and Tekkaya, A. E., 2019, "Stress State Analysis of Radial Stress Superposed Bending," International Journal of Precision Engineering and Manufacturing, **20**(1), pp. 53–66.

[20] Becker, C., Tekkaya, A. E., and Kleiner, M., 2014, "Fundamentals of the Incremental Tube Forming Process," CIRP Annals, **63**(1), pp. 253–256.

[21] Olson, G. B., 2002, "Effects of Stress and Deformation on Martensitic Formation," *Encyclopedia of Materials: Science and Technology*, Elsevier.

[22] Hecker, S. S., Stout, M. G., Staudhammer, K. P., and Smith, J. L., 1982, "Effects of Strain State and Strain Rate on Deformation-Induced Transformation in 304 Stainless Steel: Part I. Magnetic Measurements and Mechanical Behavior," Metallurgical Transactions A, **13**(4), pp. 619–626.

[23] Shen, Y. F., Li, X. X., Sun, X., Wang, Y. D., and Zuo, L., 2012, "Twinning and Martensite in a 304 Austenitic Stainless Steel," Materials Science and Engineering: A, **552**, pp. 514–522.

[24] Talyan, V., Wagoner, R. H., and Lee, J. K., 1998, "Formability of Stainless Steel," Metallurgical and Materials Transactions A, **29**(8), pp. 2161–2172.

[25] Iwamoto, T., Tsuta, T., and Tomita, Y., 1998, "Investigation on Deformation Mode Dependence of Strain-Induced Martensitic Transformation in Trip Steels and Modelling of Transformation Kinetics," International Journal of Mechanical Sciences, **40**(2), pp. 173–182.

[26] Lebedev, A. A., and Kosarchuk, V. V, 2000, "Influence of Phase Transformations on the Mechanical Properties of Austenitic Stainless Steels," International Journal of Plasticity, **16**(7), pp. 749–767.

[27] Kim, H., Lee, J., Barlat, F., Kim, D., and Lee, M.-G., 2015, "Experiment and Modeling to Investigate the Effect of Stress State, Strain and Temperature on Martensitic Phase Transformation in TRIP-Assisted Steel," Acta Materialia, **97**, pp. 435–444.

[28] Han, H. N., Lee, C. G., Oh, C.-S., Lee, T.-H., and Kim, S.-J., 2004, "A Model for Deformation Behavior and Mechanically Induced Martensitic Transformation of Metastable Austenitic Steel," Acta Materialia, **52**(17), pp. 5203–5214.

[29] Olson, G. B., and Cohen, M., 1976, "A General Mechanism of Martensitic Nucleation: Part I. General Concepts and the FCC → HCP Transformation," Metallurgical Transactions A, **7**(12), pp. 1897–1904.

[30] Stringfellow, R. G., Parks, D. M., and Olson, G. B., 1992, "A Constitutive Model for Transformation Plasticity Accompanying Strain-Induced Martensitic Transformations in Metastable Austenitic Steels," Acta Metallurgica et Materialia, **40**(7), pp. 1703–1716.

[31] Santacreu, P., Glez, J., Chinouilh, G., and Fröhlich, T., 2006, "Behaviour Model of Austenitic Stainless Steels for Automotive Structural Parts," steel research international, **77**(9–10), pp. 686–691.

[32] Beese, A. M., and Mohr, D., 2011, "Effect of Stress Triaxiality and Lode Angle on the Kinetics of Strain-Induced Austenite-to-Martensite Transformation," Acta Materialia, **59**(7), pp. 2589–2600.

[33] Mansourinejad, M., and Ketabchi, M., 2017, "Modification of Olson–Cohen Model for Predicting Stress-State Dependency of Martensitic Transformation," Materials Science and Technology, **33**(16), pp. 1948–1954.

[34] Copley, S. M., and Kear, B. H., 1968, "The Dependence of the Width of a Dissociated Dislocation on Dislocation Velocity," Acta Metallurgica, **16**(2), pp. 227–231.

[35] Martin, S., Ullrich, C., and Rafaja, D., 2015, "Deformation of Austenitic CrMnNi TRIP/TWIP Steels: Nature and Role of the Ɛ−martensite," Materials Today: Proceedings, **2**, pp. S643–S646.

[36] Ullrich, C., Eckner, R., Krüger, L., Martin, S., Klemm, V., and Rafaja, D., 2016, "Interplay of Microstructure Defects in Austenitic Steel with Medium Stacking Fault Energy," Materials Science and Engineering: A, **649**, pp. 390–399.

[37] Byun, T. S., 2003, "On the Stress Dependence of Partial Dislocation Separation and Deformation Microstructure in Austenitic Stainless Steels," Acta Materialia, **51**(11), pp. 3063–3071.

[38] Wang, H., Jeong, Y., Clausen, B., Liu, Y., McCabe, R. J., Barlat, F., and Tomé, C. N., 2016, "Effect of Martensitic Phase Transformation on the Behavior of 304 Austenitic Stainless Steel under Tension," Materials Science and Engineering: A, **649**, pp. 174–183.

[39] Zecevic, M., Upadhyay, M. V, Polatidis, E., Panzner, T., Van Swygenhoven, H., and Knezevic, M., 2019, "A Crystallographic Extension to the Olson-Cohen Model for Predicting Strain Path Dependence of Martensitic Transformation," Acta Materialia, **166**, pp. 386–401.

[40] Turner, P. A., and Tomé, C. N., 1994, "A Study of Residual Stresses in Zircaloy-2 with Rod Texture," Acta Metallurgica et Materialia, **42**(12), pp. 4143–4153.

[41] Neil, C. J., Wollmershauser, J. A., Clausen, B., Tomé, C. N., and Agnew, S. R., 2010, "Modeling Lattice Strain Evolution at Finite Strains and Experimental Verification for Copper and Stainless Steel Using in Situ Neutron Diffraction," International Journal of Plasticity, **26**(12), pp. 1772–1791.

[42] Zecevic, M., and Knezevic, M., 2018, "Latent Hardening within the Elasto-Plastic Self-Consistent Polycrystal Homogenization to Enable the Prediction of Anisotropy of AA6022-T4 Sheets," International Journal of Plasticity, **105**, pp. 141–163.

[43] Zecevic, M., and Knezevic, M., 2015, "A Dislocation Density Based Elasto-Plastic Self-Consistent Model for the Prediction of Cyclic Deformation: Application to AA6022-T4," International Journal of Plasticity, **72**, pp. 200–217.

[44] Zecevic, M., Beyerlein, I. J., and Knezevic, M., 2017, "Coupling Elasto-Plastic Self-Consistent Crystal Plasticity and Implicit Finite Elements: Applications to Compression, Cyclic Tension-Compression, and Bending to Large Strains," International Journal of Plasticity, **93**, pp. 187–211.

[45] Zecevic, M., Korkolis, Y. P., Kuwabara, T., and Knezevic, M., 2016, "Dual-Phase Steel Sheets under Cyclic Tension–Compression to Large Strains: Experiments and Crystal Plasticity Modeling," Journal of the Mechanics and Physics of Solids, **96**, pp. 65–87.

[46] Zecevic, M., and Knezevic, M., 2017, "Modeling of Sheet Metal Forming Based on Implicit Embedding of the Elasto-Plastic Self-Consistent Formulation in Shell Elements: Application to Cup Drawing of AA6022-T4," JOM, **69**(5), pp. 922–929.

[47] Lichtenfeld, J. A., Van Tyne, C. J., and Mataya, M. C., 2006, "Effect of Strain Rate on Stress-Strain Behavior of Alloy 309 and 304L Austenitic Stainless Steel," Metallurgical and Materials Transactions A, **37**(1), pp. 147–161.

[48] Knezevic, M., Zecevic, M., Beyerlein, I. J., Bingert, J. F., and McCabe, R. J., 2015, "Strain Rate and Temperature Effects on the Selection of Primary and Secondary Slip and Twinning Systems in HCP Zr," Acta Materialia, **88**, pp. 55–73.

[49] Mamros, E. M. ;, Kuijer, M. B. ;, Davarpanah, M. A. ;, Baker, I. ;, and Kinsey, B. L. ;, 2021, "The Effect of Temperature on the Strain-Induced Austenite to Martensite Transformation in SS 316L during Uniaxial Tension," *International Conference on the Technology of Plasticity*.

[50] "Damask" [Online]. Available: https://damask.mpie.de.

[51] Zecevic, M., Knezevic, M., Beyerlein, I. J., and Tomé, C. N., 2015, "An Elasto-Plastic Self-Consistent Model with Hardening Based on Dislocation Density, Twinning and de-Twinning: Application to Strain Path Changes in HCP Metals," Materials Science and Engineering: A, **638**, pp. 262–274.

[52] Masson, R., Bornert, M., Suquet, P., and Zaoui, A., 2000, "An Affine Formulation for the Prediction of the Effective Properties of Nonlinear Composites and Polycrystals," Journal of the Mechanics and Physics of Solids, **48**(6), pp. 1203–1227.

[53] Bracke, L., Kestens, L., and Penning, J., 2007, "Transformation Mechanism of A'-Martensite in an Austenitic Fe–Mn–C–N Alloy," Scripta Materialia, **57**(5), pp. 385–388.

[54] Bogers, A. J., and Burgers, W. G., 1964, "Partial Dislocations on the {110} Planes in the B.C.C. Lattice and the Transition of the F.C.C. into the B.C.C. Lattice," Acta Metallurgica, **12**(2), pp. 255–261.

[55] Knezevic, M., Beyerlein, I. J., Lovato, M. L., Tomé, C. N., Richards, A. W., and McCabe, R. J., 2014, "A Strain-Rate and Temperature Dependent Constitutive Model for BCC Metals Incorporating Non-Schmid Effects: Application to Tantalum–Tungsten Alloys," International Journal of Plasticity, **62**, pp. 93–104.

[56] Franciosi, P., and Zaoui, A., 1982, "Multislip in f.c.c. Crystals a Theoretical Approach Compared with Experimental Data," Acta Metallurgica, **30**(8), pp. 1627–1637.

[57] Khadyko, M., Dumoulin, S., Cailletaud, G., and Hopperstad, O. S., 2016, "Latent Hardening and Plastic Anisotropy Evolution in AA6060 Aluminium Alloy," International Journal of Plasticity, **76**, pp. 51–74.

[58] Mecking, H., and Kocks, U. F., 1981, "Kinetics of Flow and Strain-Hardening," Acta Metallurgica, **29**(11), pp. 1865–1875.

[59] Knezevic, M., McCabe, R. J., Tomé, C. N., Lebensohn, R. A., Chen, S. R., Cady, C. M., Gray III, G. T., and Mihaila, B., 2013, "Modeling Mechanical Response and Texture Evolution of α-Uranium as a Function of Strain Rate and Temperature Using Polycrystal Plasticity," International Journal of Plasticity, **43**, pp. 70–84.

[60] Beyerlein, I. J., and Tomé, C. N., 2008, "A Dislocation-Based Constitutive Law for Pure Zr Including Temperature Effects," International Journal of Plasticity, **24**(5), pp. 867–895.

[61] Kocks, U. F., Franciosi, P., and Kawai, M., 1991, "A Forest Model of Latent Hardening and Its Application to Polycrystal Deformations," Texture, Stress, and Microstructure, **14**, pp. 1103–1114.

[62] Teodosiu, C., Raphanel, J. L., and Tabourot, L., 1993, "Finite Element Simulation of the Large Elastoplastic Deformation of Multicrystals," *Mecamat*, pp. 153–160.

[63] Knezevic, M., Beyerlein, I. J., Brown, D. W., Sisneros, T. A., and Tomé, C. N., 2013, "A Polycrystal Plasticity Model for Predicting Mechanical Response and Texture Evolution during Strain-Path Changes: Application to Beryllium," International Journal of Plasticity, **49**, pp. 185–198.

[64] Eghtesad, A., Barrett, T. J., and Knezevic, M., 2018, “Compact Reconstruction of Orientation Distributions Using Generalized Spherical Harmonics to Advance Large-Scale Crystal Plasticity Modeling: Verification Using Cubic, Hexagonal, and Orthorhombic Polycrystals,” Acta Materialia, **155**, pp. 418–432.

[65] Garion, C., Skoczeń, B., and Sgobba, S., 2006, “Constitutive Modelling and Identification of Parameters of the Plastic Strain-Induced Martensitic Transformation in 316L Stainless Steel at Cryogenic Temperatures,” International Journal of Plasticity, **22**(7), pp. 1234–1264.